

Unveiling and quantifying the topology-dependent pre-melting of nanoparticles

Marthe Bideault,^{1,2} Arnaud Allera,³ Ryoji Asahi,⁴ Jérôme Creuze,⁵ and Erich Wimmer^{6,7}

¹Materials Design SARL, 42 avenue Verdier, 92120 Montrouge, France

²ICMMO, Université Paris-Saclay, UMR 8182, 17 avenue des Sciences, 91400 Orsay, France

³ASNR/PSN-RES/SEMIA/LSMA Centre d'études de Cadarache, F-13115 Saint Paul-lez-Durance, France ^{*}

⁴Institute of Materials Innovation, Nagoya University, Nagoya 464-8603, Japan

⁵ICMMO, Université Paris-Saclay, UMR 8182, 17 avenue des Sciences, 91400 Orsay, France [†]

⁶Materials Design SARL, 42 avenue Verdier, 92120 Montrouge, France [‡]

⁷Materials Design, Inc., 12121 Scripps Summit Drive, #160, San Diego, California 92131, USA

The melting of metallic nanoparticles is governed by surface pre-melting, a phenomenon traditionally modeled as the isotropic growth of a uniform liquid shell. Challenging this classical view, we report facet-dependent surface pre-melting in hexagonal close-packed Co nanoparticles, arising from the structural heterogeneity of the nanoparticle surface. Characterizing melting in molecular dynamics simulations (500 to 6000 atoms), we observe the onset of surface mobility, starting as low as $0.2 \times T_{M,\infty}$ ($T_{M,\infty}$ being the bulk melting point), driven by the early disordering of stepped $\{01\bar{1}1\}$ facets. We found that these facets consistently melt at temperatures nearly 200 Kelvin lower than flat $\{0001\}$ facets, regardless of particle size, and relate facets melting temperatures to the nanoparticle size via a 2D extension of the Gibbs-Thomson relation. We determine a critical liquid layer thickness that triggers the melting of the entire nanoparticle, which is found to be size-dependent. Our results confirm the recent experimental observation of the surface pre-melting effect, and extend it to anisotropic particles with different facet orientations.

I. INTRODUCTION

Nanoparticles are essential components in a wide variety of fields including alloys, catalysis, electronic, optical, and magnetic materials, as well as medical applications and cosmetics. Their high surface-to-volume ratio imparts unique properties such as size-dependent optical and magnetic properties [1], increased hardness [2], and melting point depression [3, 4]. The latter is described by the Gibbs-Thomson relation [4, 5], which states that the melting point of a spherical nanoparticle is proportional to $N^{-\frac{1}{3}}$, where N is the number of atoms.

The melting behavior of nanoparticles has been extensively studied, beginning with the pioneering work of Pawlow in 1909, who assumed a global transformation characterized by a single transition temperature [6]. In 1924, Tammann and Hüttig were the first to suggest that melting was a surface phenomenon [7]. They introduced approximate temperatures at which bulk (Tammann) and surface (Hüttig) atoms begin to diffuse in a solid material with melting temperature T_M , expressed as $T_{\text{Tammann}} = 0.5 \times T_M$ and $T_{\text{Hüttig}} = 0.3 \times T_M$, respectively. Later, in 1948, Reiss and Wilson proposed a model where a thin liquid layer forms at the nanoparticle surface at lower temperatures and persists until complete melting [8]. In 1977, Couchman and Jesser introduced a model where this liquid layer grows inward toward the core [9]. A key prediction is that, as the particle size decreases, the melting transition becomes slightly

less sharp, although it remains extremely sharp even for very small particles (broadening by less than about 1 K). Subsequent experimental and theoretical studies have confirmed that nanoparticle melting is governed by surface pre-melting [3, 4, 10–12].

In surface science, it is well-established that surfaces can exhibit complete pre-melting [13], incomplete pre-melting [14], or even no pre-melting [15]. However, when modeling nanoparticles, this behavior is comparatively less explored: surface melting is often considered as a singular phenomenon, treating the entire nanoparticle surface as one entity [11, 12, 16, 17], although surfaces can consist of multiple distinct facet types. As a result, certain facets may melt faster than others, leading to surface reconstructions or phenomena worth analyzing—particularly in fields like catalysis, where nanoparticles operate at relatively high temperatures.

In this study, hexagonal close-packed (hcp) cobalt nanoparticles are used as prototypical system. They exhibit two different types of facets: stepped $\{01\bar{1}1\}$ facets and flat $\{0001\}$ facets. The corresponding surface energies are 2.13 and 2.38 J.m⁻² respectively, according to computations with a q-SNAP machine-learned interatomic potential used in the present paper [5], which was trained on density functional theory (DFT) calculations using the Perdew-Burke-Ernzerhof (PBE) functional [18]. The surface energies computed directly with DFT-PBE yield nearly the same surface energies, namely 2.13 and 2.40 J.m⁻², respectively. For comparison, the face-centered cubic (fcc) (111) surface of cobalt, which is the most stable surface for this metal, has a slightly lower surface energy of 2.07 (DFT-PBE) or 2.09 (q-SNAP) J.m⁻². However, below 700 K, cobalt favors the hexagonal lattice structure, making hcp nanoparticles stable at low temperatures.

^{*} arnaud.allera@asnr.fr

[†] jerome.creuze@universite-paris-saclay.fr

[‡] ewimmer@materialsdesign.com

This hexagonal shape is observed to be stable for sufficiently large cobalt nanoparticles, both experimentally [19] and computationally [5, 20].

Isolated nanoparticles can be simulated at the atomic scale using molecular dynamics (MD) [16] (see Methods). The main challenge for accurate MD simulations is the realism of the interatomic potential used to describe interactions between atoms. This bottleneck was recently lifted by the introduction of an accurate machine-learned interatomic potential dedicated to Co nanoparticles, which closely matches DFT-PBE calculations over a range of properties, including surface energies, phonon dispersions, phase transition temperature, melting point, vacancy formation energies and elastic coefficients [5]. Another important challenge for atomistic studies, and the primary focus of this study, is the analysis of simulation data, which requires the identification of atomic patterns representative of crystal structures or surface orientations.

To characterize crystals, algorithms such as polyhedral template matching [21], adaptive common neighbor analysis (a-CNA) [22], or bond order parameters [23, 24], provide a local and computationally efficient geometric analysis of bulk materials. These methods have also been used for the structural characterization of the surface and the melting of metallic NPs [25], along with the analysis of the radial distribution function [26], the surface coordination number [17, 27] and/or the bond length fluctuation index (also called Lindemann index) [17, 28]. The latter is a traditional measure of interatomic distance fluctuations over the neighborhood of each atom in the NP, used to identify transitions from order to disorder states, such as crystalline and liquid ones. A departure from linearity of the global Lindemann index, i.e., averaged over all atoms, or an increase above an *ad hoc* threshold is taken as the signature of a solid-liquid phase transition [17]. Recently, more sophisticated methods associating machine learning with atomic descriptors such as a-CNA [29], radial distribution functions [30] or SOAP [31–33] have been developed to overcome the major drawbacks of the previously cited standard approaches. Some of these approaches remain too sensitive to thermal fluctuations, crystal defects and large deformations appearing in NPs to be applied on surface melting [22, 34]. An approach based on ACE descriptors and a hierarchical k-means clustering achieved improved temperature stability, allowing structural analysis up to the melting of gold NPs [35].

Modern MD simulations based on machine-learned potentials rely on high dimensional representations of local atomic environments using atomic descriptors [31, 36], which are becoming routinely used for atomic structure recognition, encouraging the development of descriptor-based methods designed to achieve improved robustness against thermal fluctuations [37–40]. These methods use descriptors such as the widely used BSO(4) bispectral descriptor functions [36], to encode atomic neighborhoods as feature vectors \mathbf{v} of dimension d , typically $d = 55$ for

BSO(4) descriptors using $j_{max} = 4$. These descriptors can be robustly compared to distributions of interest following Gorayeva *et. al.* using distortion scores [39] based on the analysis of Mahalanobis distances (see the Methods section). This approach allows the characterization of e.g., crystal defects in solids by measuring how much an atomic environment deviates from predefined statistical distributions, while being robust to fluctuations. This method, primarily aimed at the detection and analysis of structural defects in crystals, uses statistical distances to reference distributions, that are assumed to be unimodal multivariate Gaussians. The method has yet to be extended to more complex systems where distributions consisting of many modes where various population sizes coexist.

In this study, we adapt the distortion score method to analyze the inhomogeneous melting of hcp cobalt nanoparticles ranging from 587 to 6847 atoms. Qualitatively, we observe that atoms of the $\{01\bar{1}1\}$ facets are mobile even at low temperature, with vertex atoms beginning to diffuse on top of these facets around 400 K. In contrast, the denser $\{0001\}$ facets remain stable and organized up to significantly higher temperatures. The purpose of this study is to propose a quantitative analysis of this differential surface melting. Using robust analysis methods, we investigate the onset of surface melting with atomic resolution, and examine how nanoparticle size affects this behavior.

Our analysis protocol consists of two simple steps and does not rely on external pretraining or manual data labeling. First, we use unsupervised machine-learning algorithms to establish statistical distributions for each atomic environment present at low temperature, including atoms in the core, at $\{01\bar{1}1\}$ and $\{0001\}$ facets, edges, and vertices. We then classify atoms during heating trajectories, based on these predefined categories. Atoms that significantly differ from these classes (with respect to the Mahalanobis distance) are noted as outliers, or non-crystalline environments. We will see that the use of the distortion score avoids the need for defining *ad hoc* distance cut-offs to separate different classes of atomic environments, which can be viewed as a true improvement for structural analysis.

The following sections are organized as follows: we begin by exploring the global melting behavior of hcp cobalt nanoparticles and validating our approach. Then, we present a detailed analysis of differential surface melting. Our quantitative approach allows us to determine the scaling with the number of atoms, which is well captured by an extension of the Gibbs-Thomson relation. We provide a comprehensive description of the simulation and analysis methods used in this study in the Methods section.

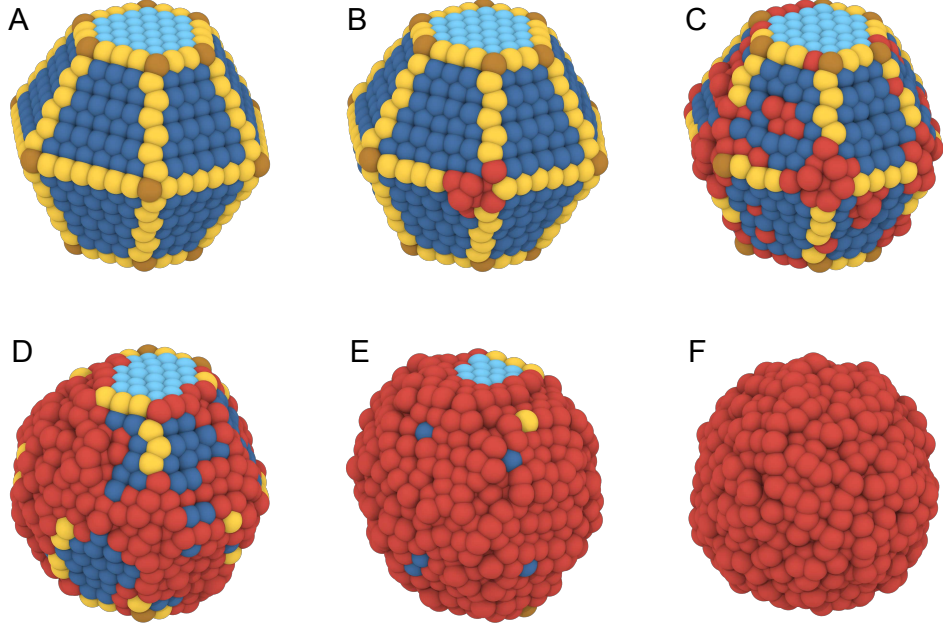


FIG. 1. Facet-dependent surface pre-melting in a 1483 atoms hexagonal close-packed cobalt nanoparticle during a heating simulation. Snapshots are taken at 0 K (A), 370 K (B), 750 K (C), 1000 K (D), 1260 K (E) and 1380 K (F), which is the melting point. Atoms belonging to $\{0001\}$ facet are colored in light blue, those from $\{01\bar{1}\}$ facet in dark blue, edge atoms are yellow and vertices are brown. Atoms that does not belong to any class are colored in red: they are outliers.

II. RESULTS

A. Classification of atoms

A crucial first step is to define classes of local atomic environments that can be tracked along an MD trajectory of an hcp nanoparticle. This task is challenging due to the complex geometry and lack of symmetry in nanoparticles. In contrast to simple periodic crystals—where symmetrically equivalent atoms typically produce unimodal descriptor distributions [39]—the diverse positions of surface atoms on a nanoparticle result in non-equivalent local environments, even within the same crystallographic facet or edge.

To address this situation, we adopt an unsupervised approach based on Gaussian Mixture Models (GMMs). While GMMs can in principle address multimodality by using several classes k , this becomes difficult in practice due to class imbalance: for example, only 18 atoms belong to the vertex class (frame A of Fig. 1), while up to 4061 atoms belong to the bulk class. Without additional assumptions or regularization, fitting many components would be unreliable.

We therefore take advantage of the naturally hierarchical distribution of nanoparticle environments—such as facets, edges, and vertices forming part of a broader surface atoms class (see frame A of Fig. 1)—to implement

an iterative classification suitable for imbalanced multimodal distributions. This iterative approach achieves a stratified decomposition of the descriptor space, using local Gaussians to approximate the multi-scale structure of the data distribution. The entire hierarchy is illustrated in Fig. S1. Similarly, Ref. [41] addressed multimodality using a K -dimensional extension of the Mahalanobis distance, on which GMM clustering was applied. However, we found that a direct hierarchical approach performed better in the present case.

After identifying reference distributions at low temperature, we analyze MD trajectories by comparing local atomic environments to these reference classes using a statistical distance criterion. Specifically, we apply a Mahalanobis distance threshold to distinguish in-distribution and out-of-distribution samples [39]. Environments with large distances to all known classes are flagged as outliers, representing configurations not encountered at low temperature. For instance, when a vertex atom migrates across the $\{01\bar{1}\}$ surface, it—and nearby surface atoms—are classified as outliers (see Fig. 1B). As the nanoparticle melts, the number of outlier atoms increases, eventually encompassing the entire system (see Fig. 1F).

This flexible method allows for a robust analysis of complex, high-temperature behavior—such as diffusion, defects, and local disorder—where rigid labels like *crystalline* or *melted* become ambiguous. Fig. 1 illustrates this

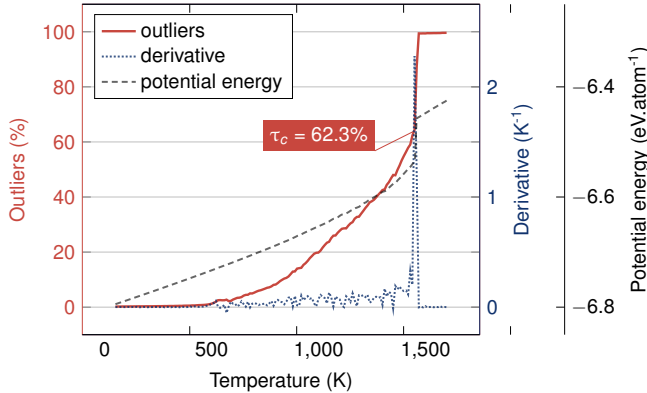


FIG. 2. Percentage of outliers (plain red line) and its derivative (dotted blue line) as a function of temperature, for a 3009 atoms hcp nanoparticle. The melting temperature corresponds to the maximum of the derivative, which is 1450 K for this hcp nanoparticle. τ_c is the maximum percentage of outliers after which the entire nanoparticle melts. The gray dashed line correspond to potential energy of the system.

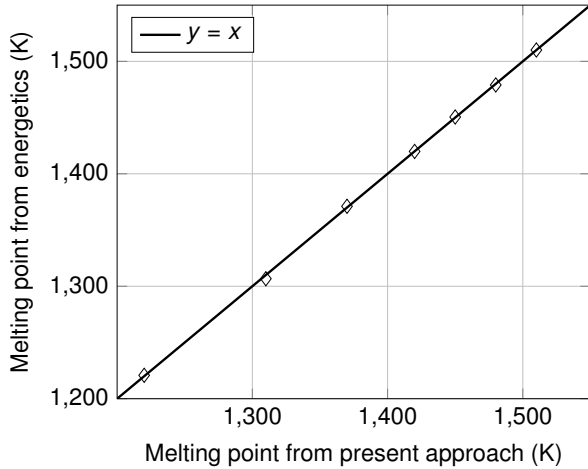


FIG. 3. Correlation between melting point from the present structural approach and from energetics, i.e., the maximum of the heat capacity.

evolution through representative snapshots at increasing temperatures, from 0 to 1380 K.

B. Global melting

Upon heating, nanoparticles undergo structural transformations from a crystalline arrangement to a liquid state with surface pre-melting playing a critical role. In this study, hcp nanoparticles were typically heated from 50 to 1600 K using molecular dynamics simulations (see Methods). Atoms were classified based on the structural distributions established at training temperatures between 50 and 400 K. Atoms that could not be assigned to these classes were labeled as outlier atoms. Starting

above 400 K, where surface diffusion begins, the fraction of outlier atoms (with respect to the entire nanoparticle) increases, reflecting atomic rearrangements on the surface, as illustrated in Fig. 1. Starting at about 600 K, the percentage of outliers increases with a fairly constant slope with rising temperature before a sudden steep increase signals the complete melting of the nanoparticle. The temperature at which the first derivative of the outlier fraction reaches a maximum is defined as the global melting temperature T_M , as shown in Fig. 2. The melting temperature derived with this method is in excellent agreement with that obtained from the maximum of the heat capacity, as demonstrated in Figs. 2 and 3. We define τ_c as the critical fraction of outlier atoms reached at T_M before the entire nanoparticle melts.

Both experimental [4] and computational [42] studies have shown that the melting temperature of a material can be estimated by analyzing nanoparticles of varying sizes. As the size increases, the melting temperature of the nanoparticle approaches that of the bulk. This phenomenon is captured by the Gibbs-Thomson relation [4]:

$$T_{m,NP} = T_{m,\infty} \left(1 - \frac{C}{D} \right), \quad (1)$$

where $T_{m,NP}$ is the melting temperature of a nanoparticle of diameter D , $T_{m,\infty}$ is the bulk melting temperature, and C is a material-dependent constant. Assuming spherical nanoparticles, we deduce that $N^{-\frac{1}{3}}$ scales with $T_{m,NP}$:

$$T_{m,NP} = T_{m,\infty} - aN^{-\frac{1}{3}}, \quad (2)$$

with $a = T_{m,\infty} \times C \left(\frac{\pi}{6} \right)^{\frac{1}{3}}$. As shown in Fig. 4, this relation is extremely well satisfied, with melting temperatures

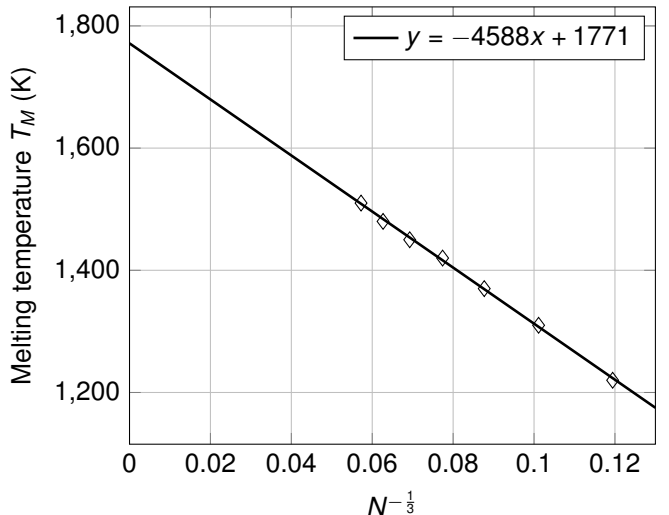


FIG. 4. Linear regression of the melting points of nanoparticles as a function of $N^{-\frac{1}{3}}$, where N is the number of atoms. The curve intersect the y axis at 1771 K.

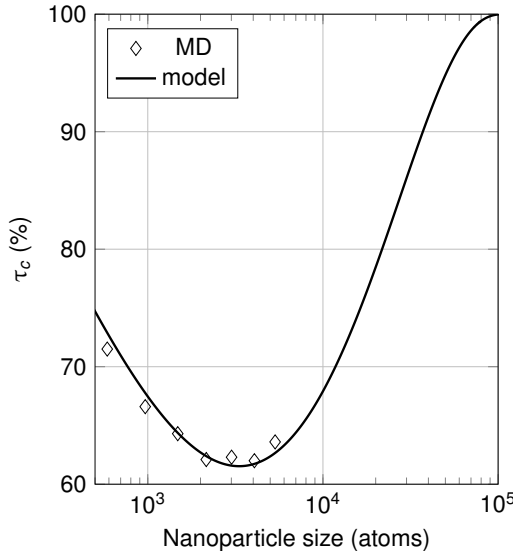


FIG. 5. Critical percentage of outliers after which the entire nanoparticle melts for nanoparticles of increasing size. The MD results are plotted with diamond symbols, and the model is an analytical function discussed in the next section.

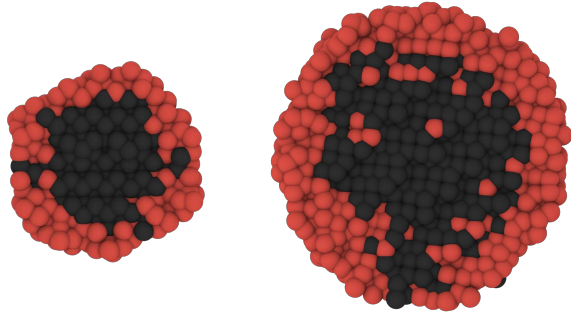


FIG. 6. Snapshot taken before the melting of (100) slices of hcp nanoparticles of 1483 (left) and 5333 (right) atoms. Red atoms are outliers, black ones are not. The thickness of the liquid layer (external red layer) increases with nanoparticle size.

decreasing linearly with $N^{-\frac{1}{3}}$. The linear fit intersects the y -axis at $T = 1771$ K, which can be interpreted as the infinite size limit, i.e., the bulk melting temperature of hcp cobalt.

The experimental melting point of Co is 1770 K [43], which refers to fcc cobalt, as cobalt undergoes an allotropic transition from hcp to fcc around 700 K [43]. Hence, the very close match of the above computed melting temperature with experimental data has to be viewed as somewhat fortuitous. However, hcp and fcc Co should not have very different melting temperatures since both structures are similar. In fact, the bulk fcc Co melting point was estimated to be 1785 K using the Gibbs-Thomson relation in our previous study [5].

As shown in Fig. 2, there is a critical percentage of out-

liers, denoted as τ_c , beyond which the entire nanoparticle melts. This quantity was computed for all the studied nanoparticles, and plotted in Fig. 5. It turns out that τ_c has a strong dependency on the nanoparticle size and reaches a minimum around $N = 3000$ atoms. On the other hand, the thickness of the liquid layer observed just before melting increases with the nanoparticle size, as shown in Fig. 6. Indeed, melting of the entire NP cannot occur before the surface melting reaches τ_c . This behavior is further discussed in the following section.

C. Surface melting

The analysis of the melting of hcp nanoparticles, treated so far globally, can be further refined. Hcp nanoparticles have two types of facets, namely flat $\{0001\}$ facets and stepped $\{01\bar{1}1\}$ facets, as illustrated in Fig. 1. The present method enables one to identify the melting of each facet independently. Fig. 7 shows the percentage of atoms that remain within their facets as a function of temperature for a 4061 atom nanoparticle. For both facets, the evolution of the fraction of atoms exhibits a continuous decrease, with a sigmoid-shaped curve. For each size, these data were fitted using the following sigmoid function:

$$\frac{n_{at \in facet}(T)}{n_{at \in facet}(T = 0 \text{ K})} = -\frac{L}{1 + e^{-k(T - T_c)}} + b, \quad (3)$$

where L , k , b and T_c are fitting parameters. The temperature corresponding to the maximum slope of the sigmoid function is termed the characteristic temperature T_c . The onset melting temperature, T_{80} , is defined as the lowest temperature at which more than 80% of the atoms remain

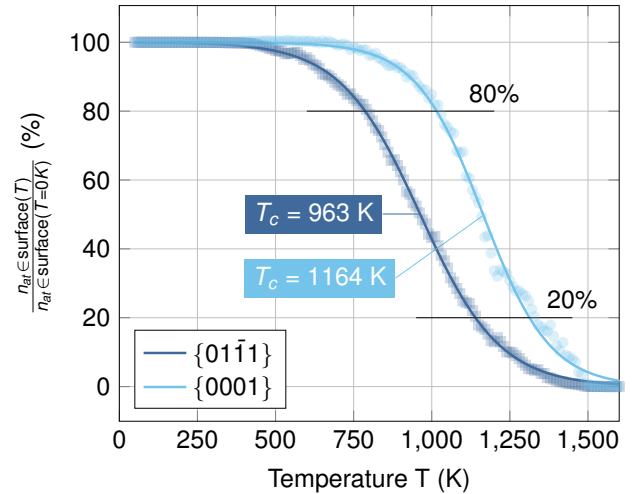


FIG. 7. Percentage of atoms that belong to $\{01\bar{1}1\}$ (dark blue) and $\{0001\}$ (light blue) facets. Plain lines correspond to sigmoid fit of these data. Characteristic temperatures T_c are indicated for each surface. The melting range $[T_{80}; T_{20}]$ is defined as the interval between 80 % and 20 % in the vertical axis.

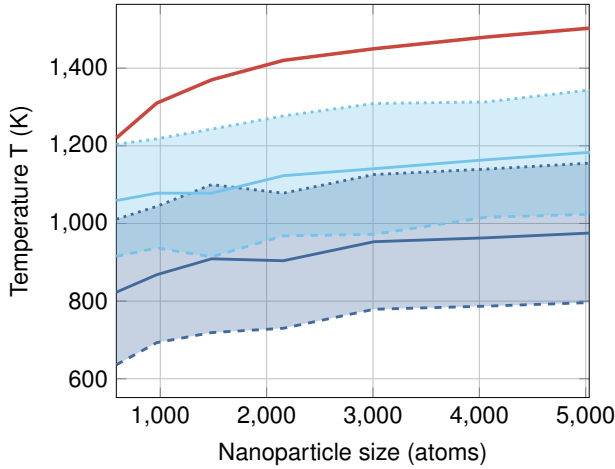


FIG. 8. Melting intervals of $\{01\bar{1}1\}$ (dark blue) and $\{0001\}$ (light blue) facets. Dashed lines correspond to the onset melting temperatures T_{80} , plain lines to characteristic temperatures T_c and dotted lines to final melting temperatures T_{20} . The red line corresponds to global melting temperatures.

within their facets. The final melting temperature, T_{20} , is the highest temperature at which less than 20% of the atoms are still within their facets. We did not take values closer to 100 and 0 % to avoid flat regions of the curves, where uncertainties on temperatures would be larger.

Melting intervals, denoted as $[T_{80}; T_c; T_{20}]$, are plotted for all nanoparticles in Fig. 8. The widths of these intervals remain relatively constant with nanoparticle size, about 320 and 360 K for $\{0001\}$ and $\{01\bar{1}1\}$, respectively. Similarly, the difference between the characteristic temperatures remains constant irrespective of the nanoparticle size, with a value of 205 K.

Fig. 8 clearly demonstrates that the smallest nanoparticle of 587 atoms melts once its $\{0001\}$ facets are entirely melted, since $T_c \approx T_{20}$. For larger nanoparticles, we have already shown that global melting is observed once the percentage of the outliers reaches τ_c , thus involving not only surface atoms (see Fig. 6 and the fact that $T_c > T_{20}$). Therefore, the global melting of hcp Co nanoparticles exhibits two different behaviors, depending on their size:

- For the smallest ones, the $\{0001\}$ facets provide additional stability to the entire nanoparticle, and global melting can occur only if these facets are melted.
- For the larger ones, in line with Couchman and Jesser's model [9], a thin liquid layer forms before global melting, which becomes thicker with the nanoparticle size.

We also show that the Gibbs-Thomson relation holds in two dimensions by using the characteristic temperatures (T_c) and the inverted square root of the number of facet atoms ($n_{(hkil)}^{-1/2}$) (value at 0 K) instead of the total number of atoms in a nanoparticle. Corresponding linear

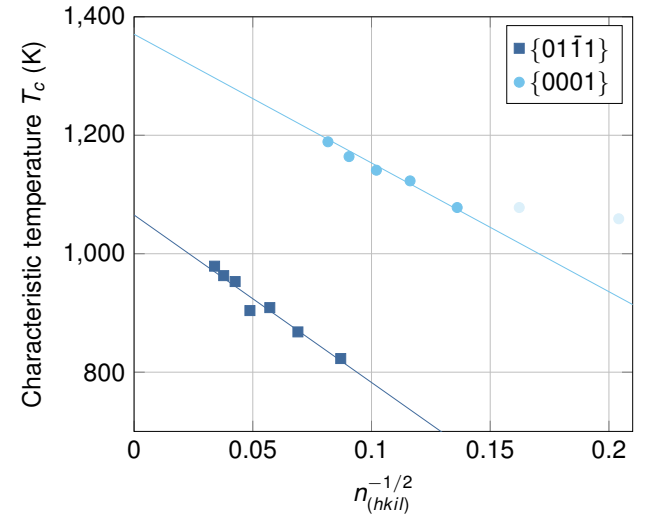


FIG. 9. Linear regression of the characteristic temperatures of $\{01\bar{1}1\}$ (squares) and $\{0001\}$ (circles) facets as a function of $n_{(hkil)}^{-1/2}$, where $n_{(hkil)}$ is the number of atoms in the corresponding $(hkil)$ facet. Characteristic temperatures of the two smallest nanoparticles (shaded here) were excluded from the linear fit for the melting of $\{0001\}$ facets. Temperatures corresponding to $n_{(hkil)} \rightarrow +\infty$ are 1065 K and 1371 K for $\{01\bar{1}1\}$ and $\{0001\}$ facets, respectively.

regressions are presented in Fig. 9. For infinite surfaces, this approach predicts melting temperatures $T_{c,\infty}$ of 1065 and 1371 K for $\{01\bar{1}1\}$ and $\{0001\}$ surfaces, respectively. However, it is important to note that facet melting in nanoparticles is induced by edges and vertices. Consequently, the melting temperature of a perfect infinite surface should be higher than these values.

D. Discussion

Here we extend the discussion of the Gibbs-Thomson relations observed in the present simulations. In the three-dimensional case, the melting temperature in Eq. 2 is rewritten in the spherical approximation as

$$T_M = T_{M,\infty} + \frac{a'}{R} \quad (4)$$

where R is the radius of the nanoparticle and $T_{M,\infty}$ is the melting temperature of bulk Co.

In the two-dimensional case, the observation in Fig. 9 leads to a similar Gibbs-Thomson relation

$$T_{c,(hkil)} = T_{c,(hkil)\infty} - b n_{(hkil)}^{-\frac{1}{2}} \quad (5)$$

where $T_{c,(hkil)}$ is the characteristic melting temperature of the $\{hkil\}$ facet containing $n_{(hkil)}$ atoms, and $T_{c,(hkil)\infty}$ is the characteristic temperature of the infinite surface with Miller indices $(hkil)$. The area A of the $(hkil)$ facet

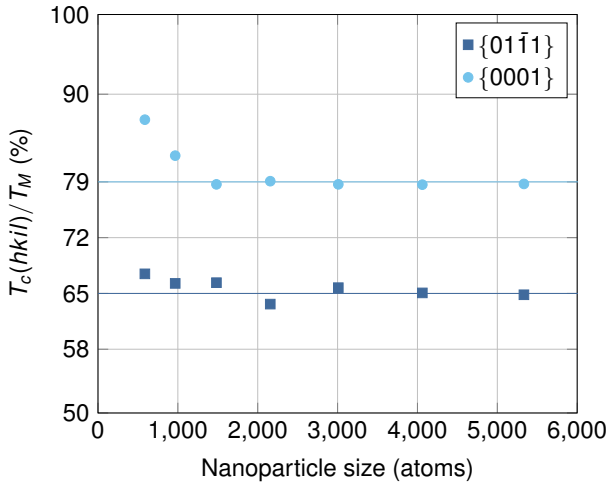


FIG. 10. Characteristic ratio of surface-to-NP melting temperature for $\{01\bar{1}1\}$ (squares) and $\{0001\}$ (circles) facets. Average values for $\{01\bar{1}1\}$ and $\{0001\}$ facets of hcp nanoparticles containing more than 1000 atoms are 65 % and 79 % respectively.

can be expressed using the solid angle Ω :

$$A_{(hkil)} = R^2 \Omega. \quad (6)$$

As $A_{(hkil)}$ is proportional to $n_{(hkil)}$, $n_{(hkil)}$ is proportional to R^2 and we get

$$T_{c,(hkil)} = T_{c,(hkil)\infty} + \frac{b'}{R}. \quad (7)$$

Dividing Eq. 7 by Eq. 4 gives

$$\frac{T_{c,(hkil)}}{T_M} = \frac{T_{c,(hkil)\infty} + b'x}{T_{M,\infty} + a'x} \quad (8)$$

where $x = \frac{1}{R}$. The Taylor expansion around $x = 0$ gives

$$\frac{T_{c,(hkil)}}{T_M} = \frac{T_{c,(hkil)\infty}}{T_{M,\infty}} + \frac{d}{R} + \mathcal{O}\left(\frac{1}{R^2}\right) \quad (9)$$

where $d = \frac{b'T_{M,\infty} - a'T_{c,(hkil)\infty}}{T_{M,\infty}^2}$.

We investigated the ratio T_c/T_M for each facet and plotted it in Fig. 10 as a function of the NP size. As expected from Eq. 9, the ratios T_c/T_M become independent of the NP size when R is large. Reading Figs. 4 and 9 for each facet at a larger NP size, we found $\frac{T_{c,(01\bar{1}1)\infty}}{T_{M,\infty}} = 0.60$

and $\frac{T_{c,(0001)\infty}}{T_{M,\infty}} = 0.77$, respectively. These values closely match the average trends shown in Fig. 10, reinforcing the relevance and validity of adapting the Gibbs-Thomson relation to two-dimensional systems.

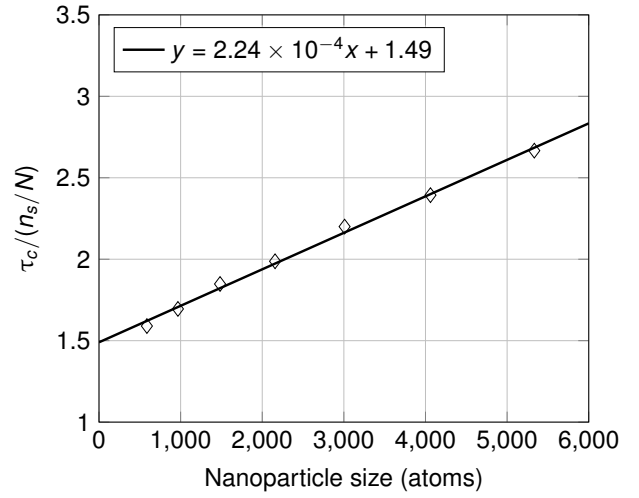


FIG. 11. The NP size dependency of the critical number of liquid layers, $\tau_c/(n_s/N) = l_c$.

Thus, for sufficiently large nanoparticles, the constant T_c/T_M ratio indicates that nanoparticles consistently reach their characteristic temperature T_c at a fixed percentage of their melting temperature. The fact that $\{01\bar{1}1\}$ facets melt before $\{0001\}$ is consistent with energetics, as the surface energy of the $\{0001\}$ facet is lower than that of $\{01\bar{1}1\}$ (2.13 J.m^{-2} compared to 2.38 J.m^{-2}). This staged surface melting behavior is very similar to the one observed for the roughening transition of metallic (macroscopic) crystal surfaces [44].

Regarding the critical percentage of outliers τ_c , we can express it using the critical number of liquid layers of the surface, l_c , as

$$\tau_c = n_0/N = n_s l_c/N, \quad (10)$$

where n_0 is the number of outliers and n_s is the number of surface atoms at $T = 0$. Thus, $\tau_c/(n_s/N) = l_c$. Rescaling τ_c in Fig. 5, we obtained Fig. 11. As observed in Fig. 6, the critical number of liquid layers indeed monotonically increases with the NP size in the range of nanoparticle sizes under investigation.

Once we assume the linear relation of l_c with N , we reproduce the minimum behavior of τ_c in Fig. 5 as described here. The critical percentage of outliers, defined as $\tau_c = \frac{n_0}{N}$ where n_0 is the number of atoms classified as outliers and N is the NP total number of atoms, can be expressed in terms of the NP radius R within the spherical approximation as

$$\tau_c = \frac{n_0}{N} = \frac{1}{v_0} \int_{R-t_c}^R 4\pi r^2 dr / \frac{4\pi R^3}{3v_0} \quad (11)$$

$$= \frac{1}{R^3} \{R^3 - (R - t_c)^3\} \quad (12)$$

$$= 1 - (1 - t_c/R)^3. \quad (13)$$

Here, t_c is the critical thickness of the liquid NP shell ($t_c \leq R$) and v_0 is the unit volume per atom, V/N . Now,

we define a unit size of Δ_v for an atom satisfying $v_o = \Delta_v^3$, and a layer thickness along the nanoparticle radius, Δ_r , leading to

$$t_c = l_c \Delta_r, \quad (14)$$

$$R = \left(\frac{3N}{4\pi} \right)^{1/3} \Delta_v, \quad (15)$$

where l_c is the critical number of liquid layers of the NP shell. Then,

$$t_c/R = \frac{l_c \Delta_r}{\left(\frac{3N}{4\pi} \right)^{1/3} \Delta_v} \quad (16)$$

$$= \left(\frac{3N}{4\pi} \right)^{-1/3} l_c \delta. \quad (17)$$

Here, we introduce $\delta = \Delta_r/\Delta_v$, which is expected to be around one, but taken to be an adjustable parameter considering arbitrariness of quantifying these unit sizes in real nanoparticles. So Eq. 13 becomes

$$\tau_c = 1 - \left\{ 1 - \left(\frac{3N}{4\pi} \right)^{-1/3} l_c \delta \right\}^3. \quad (18)$$

Using the linear relation of l_c with N shown in Fig. 11 and using $\delta = 1.13$, we can model analytically the evolution of τ_c as a function of N , as shown in the solid line of Fig. 5. The result shows good agreement with the present MD results; it has a minimum for τ_c around $N = 3000$ and reaches 100 % for large nanoparticles, illustrating the existence of the critical liquid NP shell as a unique feature of relatively small nanoparticles.

We should note that the above assumption of the linear relation of l_c with N is not verified for the largest nanoparticle ($N > 6000$ atoms) in the present simulations. Further investigations are required to clarify this issue.

The above discussion is consistent with the model of Couchman and Jesser [9] and can be thought of as a wetting of the solid core by a liquid shell at $T < T_M$ in a metastable state. They found that the wetting is limited due to the finite size of the nanoparticle, and the critical liquid thickness is not constant but increases monotonically with increasing particle size. This has been observed experimentally very recently for Sn nanoparticles [45] and is similar to the behavior modeled in the context of surface segregation in bimetallic nanoparticles [46].

Finally, we note an advantage of the present algorithm to describe the nanoparticle melting with far greater precision than traditional approaches such as a-CNA [22], PTM [21], or the Lindemann criterion [47].

The robustness of machine-learning-based analysis methods against thermal noise is now well established [37–40]. However, the materials studied previously often possessed a majoritary distribution (e.g., defects in bulk) and a reduced diversity of atomic environments. Furthermore, when using the Mahalanobis distance, a key

assumption is that the statistical distributions of atomic environments are unimodal Gaussians [39], which is not rigorously verified in the present case. The lack of periodicity and the small sizes of the systems studied thus made their analysis particularly challenging.

In the classification used in this paper, all atoms of a given facet type are grouped in the same class. For instance, an atom located next to the edge of an $\{01\bar{1}1\}$ facet is assigned to the $\{01\bar{1}1\}$ facet's class, as well as an atom located in the center of the same facet. Further decomposing the $\{01\bar{1}1\}$ facet's class into several classes using the GMM algorithm could reveal the presence of several sub-distributions, allowing to separate atoms to reflect differences on their local environment. This suggests that a finer granularity of analysis would be straightforward to achieve using the same workflow, allowing the analysis of local atomic patterns found on surfaces. In the present work, we avoided excessively multiplying the number of classes, and chose to work with classes that do not rigorously adhere to the unimodality condition. The fact that our classification performs well, even for non-unimodal classes, further underscores the robustness and flexibility of these methods, two characteristics that are clear limitations of more traditional analysis techniques such as PTM [21] or a-CNA [22].

E. Conclusion

This study has quantified the complex surface pre-melting and global melting behavior of hexagonal close-packed cobalt nanoparticles containing between 500 and 6000 atoms. The results highlight the significance of the crystallographic orientation of surface facets in this process. Using a machine-learning-based classification method, we demonstrated that stepped $\{01\bar{1}1\}$ facets consistently melt before flat $\{0001\}$ facets, regardless of nanoparticle size. The melting temperature ranges and differences between these facets remain invariant with size, although the overall melting behavior depends on nanoparticle size following the classical Gibbs-Thomson law.

Remarkably, we found that (i) atoms located in vertices start diffusing well below the melting temperature, near 400 K, which is close to ambient conditions, (ii) there exists a critical percentage of outliers, i.e., atoms in a structural environment that differs substantially from the low temperature ordered one, that has to be reached to allow the entire melting of the nanoparticle, the variation of this critical percentage of outliers with the nanoparticle size being non-monotonous, due to the existence of a corresponding critical thickness for the liquid layer that increases monotonically with the nanoparticle size, and (iii) for very small nanoparticles, global melting can occur only if the overall external shell including the most stable facet melts.

We extended the Gibbs-Thomson relation to surfaces,

linking facet-specific melting temperatures to nanoparticle size. Compared to traditional analysis techniques, our approach offers enhanced robustness against thermal noise and superior precision in characterizing complex atomic environments. These findings underscore the versatility of descriptor-based methods in quantifying the thermal behavior of systems with multimodal distributions of atomic environments, opening new avenues for the study of nanoparticles and their unique properties.

III. METHODS

a. Creation of nanoparticles Hexagonal close-packed nanoparticles were created using the *MedeA* materials modeling environment [48], following the protocol illustrated on Fig. 12. First, the smallest hexagon is selected inside a large hcp supercell. Then, the nearest unselected neighbor of each atom is added to the hexagon: a layer is added. This operation is repeated until the desired size is obtained.

b. Molecular dynamics simulations The heating trajectory is simulated using the LAMMPS molecular dynamics package [49] and a quadratic spectral neighbor analysis potential (q-SNAP) [50, 51] developed for bulk, surface, and nanoparticle structures of cobalt [5]. The generation of the machine-learned potential and its use with LAMMPS are integrated functionalities of *MedeA*. The heating is performed in steps of 100 ps per 10 K increment, ranging from 50 K to 1600 K. A Nosé-Hoover thermostat with a damping constant of 200 fs is employed, and the time step is set to 2 fs. The bispectrum descriptors of all atoms are saved every 2 ps. They are computed using an angular moment parameter $j_{max} = 4$ and a cut-off radius $R_{cut} = 5 \text{ \AA}$, as used in the q-SNAP potential [5] used here.

c. Structural analysis The bispectrum descriptors are used to train the classifier at low temperatures. The purpose of this initial step is to define the classes of atoms (e.g., bulk, facets, edges, and vertices). To ensure accurate classification, the training temperature must be low enough so that surface diffusion has not yet started, as diffusing atoms would no longer correspond to their

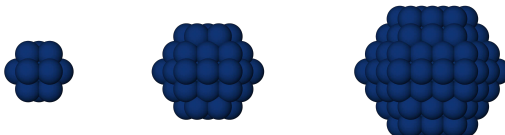


FIG. 12. Construction of hexagonal close-packed (hcp) nanoparticles using the *MedeA* materials modeling environment [48]. The process begins by selecting the smallest hexagonal motif in an hcp supercell, consisting of 13 atoms (left). Successive layers of nearest neighbors are then added to grow the nanoparticle to the desired size. The middle and right nanoparticles illustrated in this figure contain 57 and 153 atoms, respectively.

original classes. For hcp nanoparticles, this temperature is set to $T_{\max, \text{hcp}} = 400 \text{ K}$, at which vertex atoms begin to diffuse towards the edges and the $\{01\bar{1}\}$ facets. The remainder of the heating trajectory is used solely for classification.

We use unsupervised learning with Gaussian Mixture Models (GMM) to define the atomic classes in a hierarchical, binary manner. At each step, the training set is divided into two classes using two gaussians, even if the final number of classes is larger. For example, we first separate the atoms into bulk and surface. Then, one of these subsets—such as the surface atoms—is further split into two classes, and this process is repeated iteratively until all atomic classes (e.g., facets, edges, vertices) are identified. When applied to other systems, it could become difficult to intuitively determine how many iterations should be performed, which can be addressed by applying standard statistical methods for model evaluation.

The Mahalanobis distance $d_k(\mathbf{x})$ of \mathbf{x} with respect to the class k with empirical mean μ_k and covariance Σ_k is expressed as:

$$d_k(\mathbf{x}) = \sqrt{(\mathbf{x} - \mu_k)^\top \Sigma_k^{-1} (\mathbf{x} - \mu_k)} \quad (19)$$

Once the classes are defined, we first use the Minimum Covariance Determinant (MCD) algorithm to refine the estimates of the empirical mean and covariance matrix, which are critical parameters for Mahalanobis distances calculations, using a contamination level set to 7 % of the data [39, 52]. Then, we compute the empirical covariance Σ of each class. It allows us to determine a threshold Mahalanobis distance (or distortion score) [39] for all

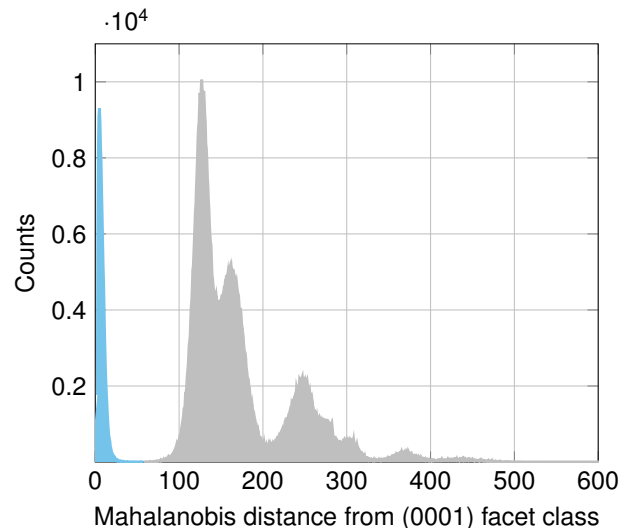


FIG. 13. Distortion scores of atoms in the training set relative to the $\{0001\}$ facet class for a 4061 atoms hcp nanoparticle. The first peak, displayed in light blue, corresponds to the atoms from $\{0001\}$ facets, whereas following gray peaks correspond to atoms from other classes.

atoms in the training set relative to each class. As shown in Fig. 13, Mahalanobis distances histograms exhibit a primary peak at short distances, corresponding to atoms that belong to the class associated with the histogram. Subsequent peaks represent atoms that do not belong to the current class. The threshold distance is automatically determined as the closest minimum to the second peak. This procedure enables the definition of a maximum statistical distance for an atom to be classified into a specific class.

The Mahalanobis distance for each atom is then computed across the entire trajectory, and atoms are classified based on these threshold distances. This classification approach is more robust than simpler binary classifiers, which always assign a class to an atom. Here, if an atom's distance exceeds all the maximum threshold distances, it is identified as an outlier. Such a classification would not be possible if we relied solely on the GMM model,

for example.

Supplementary Information

Fig. 2 and Fig. 7 are given for all nanoparticles in Supporting Information. Relevant information such as global melting points, τ_c , characteristic, onset and final temperatures for the melting of each facets are summarized in Table S1.

Acknowledgments

We gratefully acknowledge Dr. Mihai-Cosmin Marinica for his guidance in adapting the distortion score method to this study. The authors are grateful to all colleagues at Materials Design. The French Association Nationale de la Recherche et de la Technologie (ANRT) is acknowledged for CIFRE funding No. 2022/1599.

[1] Y. A. Koksharov, *Magnetic nanoparticles* , 197 (2009).

[2] D. Guo, G. Xie, and J. Luo, *J. Phys. D: Appl. Phys.* **47**, 013001 (2013).

[3] A. v. Teijlingen, S. A. Davis, and S. R. Hall, *Nanoscale Advances* **2**, 2347 (2020).

[4] S. L. Lai, J. R. A. Carlsson, and L. H. Allen, *Applied Physics Letters* **72**, 1098 (1998).

[5] M. Bideault, J. Creuze, R. Asahi, and E. Wimmer, *Phys. Rev. Mater.* **8**, 123803 (2024).

[6] P. Pawlow, *Zeitschrift für Physikalische Chemie* **65U**, 1 (1909).

[7] G. Tammann, *Zeitschrift für anorganische und allgemeine Chemie* **157**, 321 (1926).

[8] H. Reiss and I. B. Wilson, *Journal of Colloid Science* **3**, 551 (1948).

[9] P. R. Couchman and W. A. Jesser, *Nature* **269**, 481 (1977).

[10] S. L. Lai, J. Y. Guo, V. Petrova, G. Ramanath, and L. H. Allen, *Phys. Rev. Lett.* **77**, 99 (1996).

[11] A. P. Chernyshev, *Materials Chemistry and Physics* **112**, 226 (2008).

[12] K. K. Nanda, *Pramana - J Phys* **72**, 617 (2009).

[13] L. Pedemonte, G. Bracco, R. Beikler, E. Taglauer, A. Robin, and W. Heiland, *Surface Science Proceedings of the 7th International Conference on Nanometer-Scale Science and Technology and the 21st European Conference on Surface Science*, 532-535, 13 (2003).

[14] H. M. van Pinxteren and J. W. M. Frenken, *Surface Science* **275**, 383 (1992).

[15] P. Carnevali, F. Ercolelli, and E. Tosatti, *Phys. Rev. B* **36**, 6701 (1987).

[16] F. Baletto and R. Ferrando, *Rev. Mod. Phys.* **77**, 371 (2005).

[17] X. Liu, X. Wen, and R. Hoffmann, *ACS Catal.* **8**, 3365 (2018).

[18] J. P. Perdew, K. Burke, and M. Ernzerhof, *Phys. Rev. Lett.* **77**, 3865 (1996), publisher: American Physical Society.

[19] V. V. Matveev, D. A. Baranov, G. Y. Yurkov, N. G. Akatiev, I. P. Dotsenko, and S. P. Gubin, *Chemical Physics Letters* **422**, 402 (2006).

[20] B. Farkaš and N. H. de Leeuw, *Nanotechnology* **31**, 195711 (2020).

[21] P. M. Larsen, S. Schmidt, and J. Schiøtz, *Modelling Simul. Mater. Sci. Eng.* **24**, 055007 (2016).

[22] A. Stukowski, *Modelling Simul. Mater. Sci. Eng.* **20**, 045021 (2012).

[23] G. J. Ackland and A. P. Jones, *Phys. Rev. B* **73**, 054104 (2006).

[24] W. Mickel, S. C. Kapfer, G. E. Schröder-Turk, and K. Mecke, *The Journal of Chemical Physics* **138**, 044501 (2013).

[25] R. Essajai, A. Rachadi, M. Qjani, A. Mzerd, and N. Has-sanain, *Chemical Physics* **526**, 110441 (2019).

[26] L. Delgado-Callico, K. Rossi, R. Pinto-Miles, P. Salzbrenner, and F. Baletto, *Nanoscale* **13**, 1172 (2021).

[27] H. Barron, G. Opletal, R. D. Tilley, and A. S. Barnard, *Catal. Sci. Technol.* **6**, 144 (2016).

[28] A. S. Barnard, *Reports on Progress in Physics* **73**, 086502 (2010).

[29] C. Roncaglia and R. Ferrando, *Journal of Chemical Information and Modeling* **63**, 459 (2023).

[30] E. Telari, A. Tinti, M. Settem, L. Maragliano, R. Ferrando, and A. Giacomello, *ACS nano* **17**, 21287 (2023).

[31] A. P. Bartók, R. Kondor, and G. Csányi, *Phys. Rev. B* **87**, 184115 (2013).

[32] D. Rapetti, M. Delle Piane, M. Cioni, D. Polino, R. Ferrando, and G. M. Pavan, *Communications Chemistry* **6**, 143 (2023).

[33] M. Cioni, M. Delle Piane, D. Polino, D. Rapetti, M. Crippa, E. A. Irmak, S. Van Aert, S. Bals, and G. M. Pavan, *Advanced Science* **11**, 2307261 (2024).

[34] W. Z. Polak, *Computational Materials Science* **201**, 110882 (2022).

[35] C. Zeni, K. Rossi, T. Pavloudis, J. Kioseoglou, S. de Gironcoli, R. E. Palmer, and F. Baletto, *Nature Communications* **12**, 6056 (2021).

[36] A. P. Bartók, M. C. Payne, R. Kondor, and G. Csányi, *Phys. Rev. Lett.* **104**, 136403 (2010).

- [37] A. Allera, A. M. Goryaeva, P. Lafourcade, J.-B. Maillet, and M.-C. Marinica, Computational Materials Science **231**, 112535 (2024).
- [38] P. Lafourcade, J.-B. Maillet, C. Denoual, E. Duval, A. Allera, A. M. Goryaeva, and M.-C. Marinica, Computational Materials Science **230**, 112534 (2023).
- [39] A. M. Goryaeva, C. Lapointe, C. Dai, J. Dérès, J.-B. Maillet, and M.-C. Marinica, Nat Commun **11**, 4691 (2020).
- [40] T. D. Swinburne, Phys. Rev. Lett. **131**, 236101 (2023).
- [41] A. E. Poisvert, C. Lapointe, A. M. Goryaeva, L. Kurpaska, J. S. Wróbel, and M.-C. Marinica, Physical Review Materials **9**, 093604 (2025).
- [42] P. Buffat and J.-P. Borel, Phys. Rev. A **13**, 2287 (1976), publisher: American Physical Society.
- [43] A. Fernández Guillermet, Int J Thermophys **8**, 481 (1987).
- [44] J. Lapujoulade, Surface Science Reports **20**, 195 (1994).
- [45] A. Kryshtal, S. Bogatyrenko, and O. Khshanovska, Nano Letters **23**, 6354 (2023), pMID: 37418684.
- [46] J. Creuze, F. Berthier, and B. Legrand, Segregation and phase transitions in reduced dimension: From bulk to clusters via surfaces, in *Nanoalloys: Synthesis, Structure and Properties*, edited by D. Alloyeau, C. Mottet, and C. Ricolleau (Springer London, London, 2012) pp. 227–257.
- [47] F. A. Lindemann, Physikalische Zeitschrift **11**, 609 (1910).
- [48] MedeA 3.8; MedeA is a registered trademark of Materials Design, Inc., San Diego, USA. (2023).
- [49] A. P. Thompson, H. M. Aktulga, R. Berger, D. S. Bolineanu, W. M. Brown, P. S. Crozier, P. J. in 't Veld, A. Kohlmeyer, S. G. Moore, T. D. Nguyen, R. Shan, M. J. Stevens, J. Tranchida, C. Trott, and S. J. Plimpton, Computer Physics Communications **271**, 108171 (2022).
- [50] A. P. Thompson, L. P. Swiler, C. R. Trott, S. M. Foiles, and G. J. Tucker, Journal of Computational Physics **285**, 316 (2015).
- [51] M. A. Wood and A. P. Thompson, J. Chem. Phys. **148**, 241721 (2018).
- [52] M. Hubert and M. Debruyne, WIREs Computational Statistics **2**, 36 (2010).

Supporting information

Unveiling and quantifying the topology-dependent pre-melting of nanoparticles

Marthe Bideault,^{1,2} Arnaud Allera,³ Ryoji Asahi,⁴ Jérôme Creuze,⁵ and Erich Wimmer^{6,7}

¹Materials Design SARL, 42 avenue Verdier, 92120 Montrouge, France

²ICMMO, Université Paris-Saclay, UMR 8182, 17 avenue des Sciences, 91400 Orsay, France

³ASNR/PSN-RES/SEMIA/LSMA Centre d'études de Cadarache, F-13115 Saint Paul-lez-Durance, France *

⁴Institute of Materials Innovation, Nagoya University, Nagoya 464-8603, Japan

⁵ICMMO, Université Paris-Saclay, UMR 8182, 17 avenue des Sciences, 91400 Orsay, France †

⁶Materials Design SARL, 42 avenue Verdier, 92120 Montrouge, France ‡

⁷Materials Design, Inc., 12121 Scripps Summit Drive, #160, San Diego, California 92131, USA

* arnaud.allera@asnr.fr

† jerome.creuze@universite-paris-saclay.fr

‡ ewimmer@materialsdesign.com

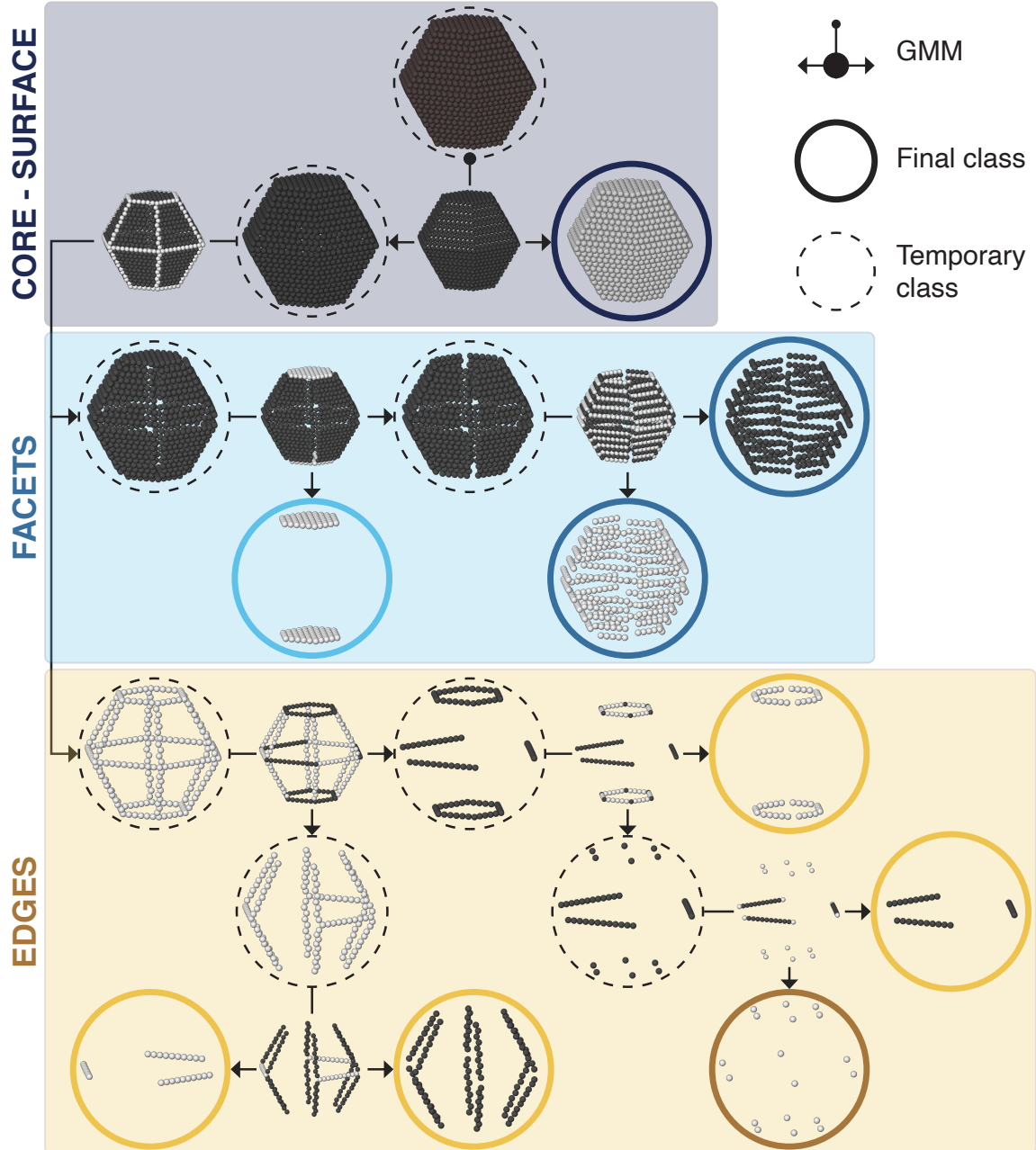


FIG. S1: Classification tree for the initial unsupervised classification using Gaussian Mixture Models (GMM). Starting from an initial nanoparticle containing unlabeled atoms, binary GMM classification is performed. The training set is separated into two subclasses (colored in black and white) by the binary GMM. The process is repeated until the classes are considered as final. Final classes corresponding to bulk, $\{0001\}$ facets, $\{01\bar{1}1\}$ facets, edges, and vertices are circled in indigo, light blue, dark blue, yellow and brown, respectively. Temporary classes (including atoms corresponding to different final classes) are circled with dashed lines.

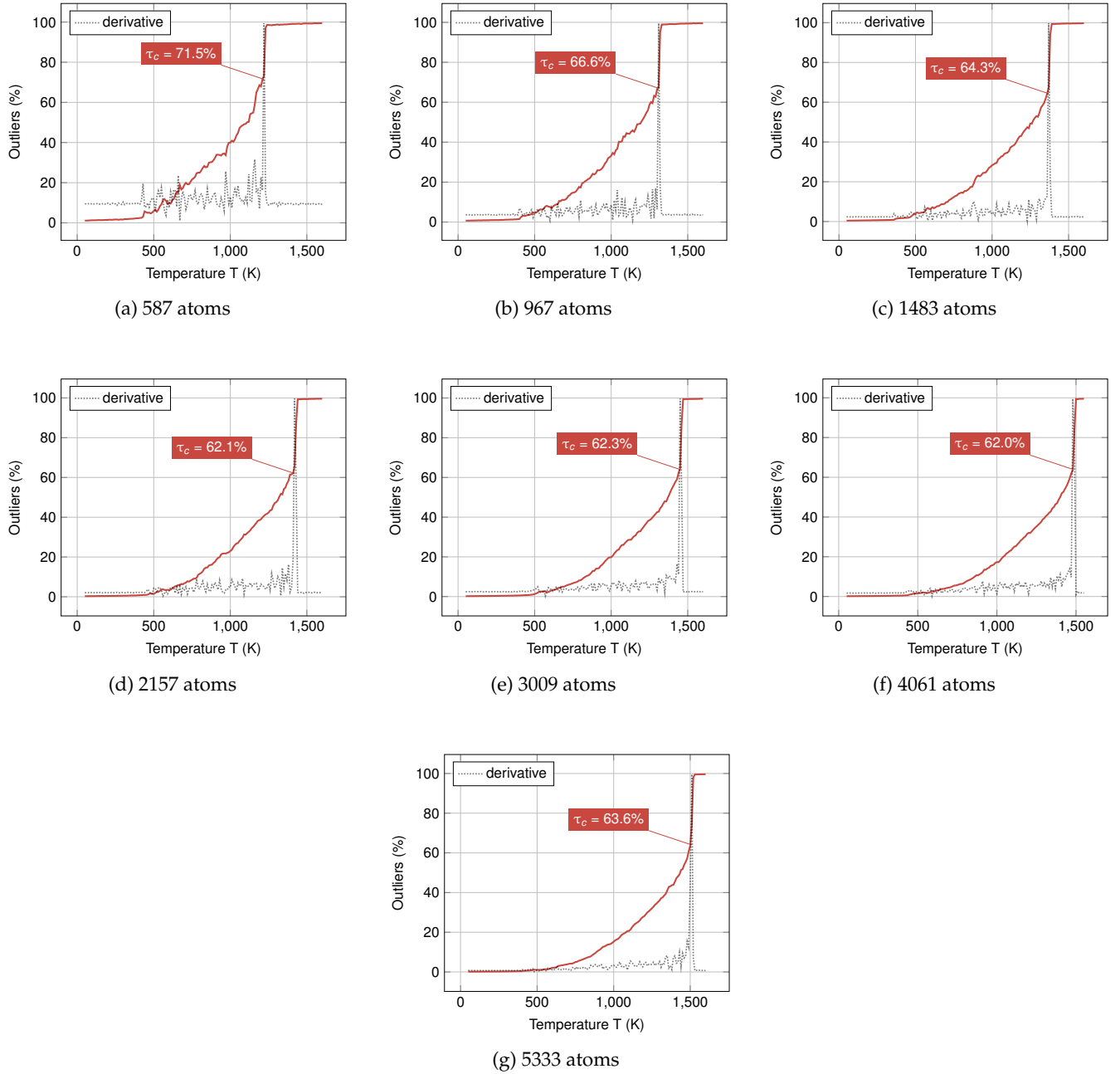


FIG. S2: Percentage of outliers (plain red line) and its derivative (dotted gray line) as a function of temperature, for all sizes of nanoparticles considered in this study. The melting temperature correspond to the maximum of the derivative. τ_c is the maximum percentage of outliers after which the entire nanoparticle melts.

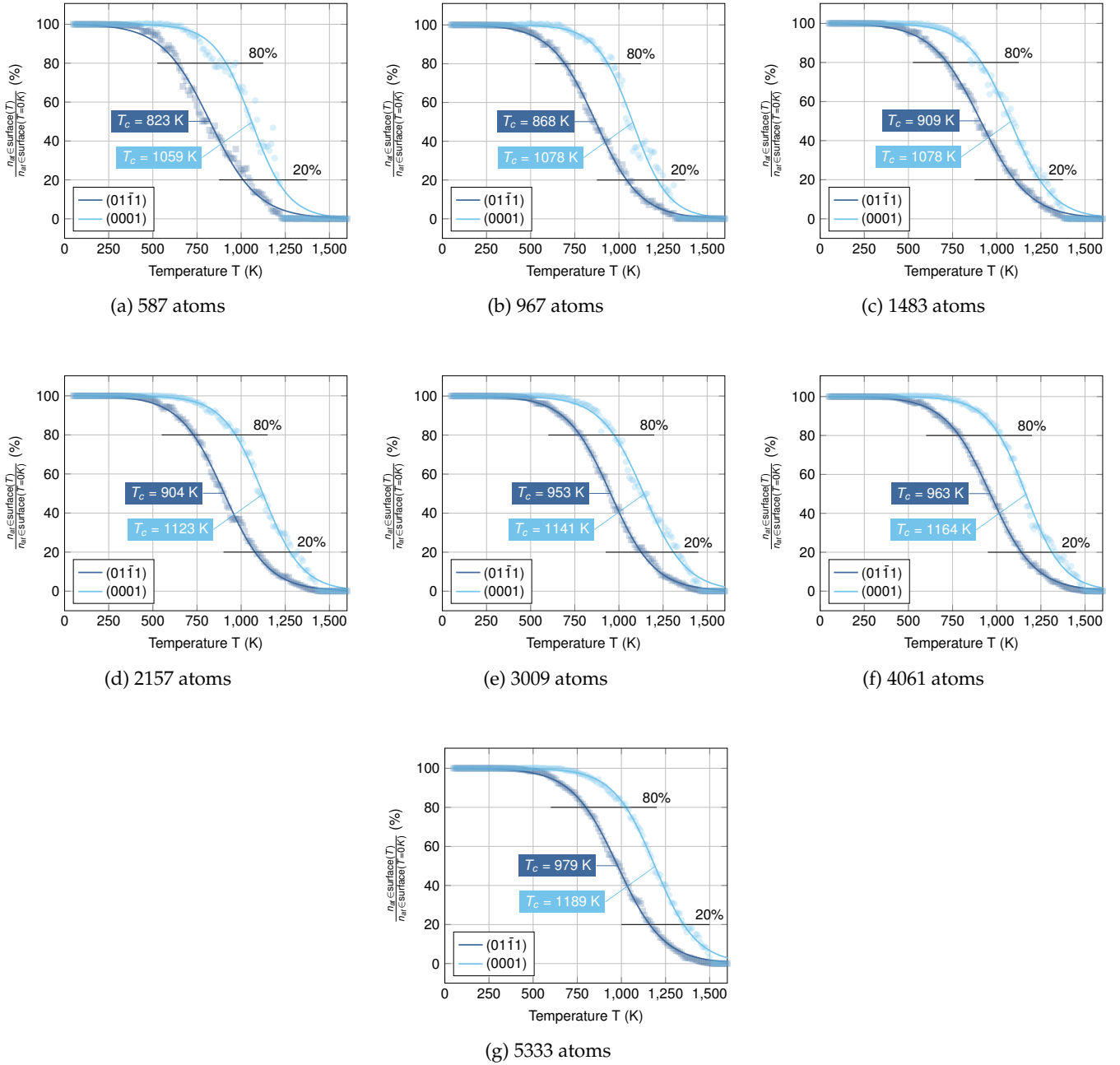


FIG. S3: Percentage of atoms that still belong to $\{01\bar{1}1\}$ (dark blue) and $\{0001\}$ (light blue) facets for all sizes of nanoparticles considered in this study. Plain lines correspond to sigmoid fit of these data. Characteristic temperatures T_c are indicated for each surface. The melting range $[T_{80}; T_{20}]$ is defined as the interval between 80 % and 20 % in the vertical axis.

TABLE S1: Relevant numerical values for each size of nanoparticle.

N^a	587	967	1483	2157	3009	4061	5333
n_c^b	323	587	967	1483	2157	3009	4061
n_s^c	264	380	516	674	852	1052	1272
T_M^d	1220	1310	1370	1420	1450	1480	1510
τ_c^e	71.5	66.6	64.3	62.1	62.3	62.0	63.6
$T_{c,(01\bar{1}1)}^f$	823	868	909	904	953	963	979
$T_{c,(0001)}^f$	1059	1078	1078	1123	1141	1164	1189
$T_{80,(01\bar{1}1)}^g$	636	693	719	730	779	787	799
$T_{80,(0001)}^g$	915	937	914	968	972	1016	1026
$T_{20,(01\bar{1}1)}^h$	1011	1044	1100	1078	1126	1140	1160
$T_{20,(0001)}^h$	1204	1218	1243	1277	1309	1313	1353

^a Number of atoms; ^b Number of core atoms; ^c Number of surface atoms; ^d Nanoparticle's melting point; ^e Critical number of outliers after which the entire nanoparticle melts; ^f Characteristic temperature for (01 $\bar{1}$ 1) and (0001) facets; ^g Lowest temperature at which more than 80% of the atoms remain in the (01 $\bar{1}$ 1) or (0001) facet's class (i.e. as onset melting temperature for the considered facet); ^h Highest temperature at which less than 20% of the atoms remain in the (01 $\bar{1}$ 1) or (0001) facet's class (i.e. final melting temperature for the considered facet);